Materials Science & Engineering C 97 (2019) 275–284

Contents lists available at ScienceDirect

Materials Science & Engineering C

journal homepage: www.elsevier.com/locate/msec

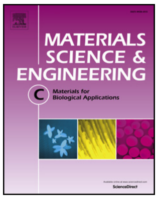

Low-modulus biomedical Ti–30Nb–5Ta–3Zr additively manufactured by Selective Laser Melting and its biocompatibility

J.P. Luo[a,b], J.F. Sun[a,*], Y.J. Huang[a], J.H. Zhang[b], Y.D. Zhang[c], D.P. Zhao[d], M. Yan[b,*]

[a] School of Materials Science and Engineering, Harbin Institute of Technology, Harbin 150001, China
[b] Department of Materials Science and Engineering, Shenzhen Key Laboratory for Additive Manufacturing of High-performance Materials, Southern University of Science and Technology of China, Shenzhen 518055, China
[c] Department of Biology, South University of Science and Technology of China, Shenzhen 518055, China
[d] College of Biology, Hunan University, Changsha 410082, China

ARTICLE INFO

Keywords:
Selective Laser Melting
TNTZ
Biocompatibility
Mechanical properties
Microstructure

ABSTRACT

Low Young's modulus titanium alloys, such as Ti-30Nb-5Ta-3Zr (TNTZ) of this study, were promising biocompatible implant materials. In this work, TNTZ samples with relative density of 96.8%–99.2% were additively manufactured by powder-bed based Selective Laser Melting (SLM) through tuning processing parameters, i.e. varying the point distance between 50 and 75 μm, laser exposure time between 135 and 200 μs, and a fixed laser power of 200 W. The microstructure, elastic properties, fatigue properties and machining accuracy of the fabricated samples have been investigated. Lattice structure TNTZ samples with porosity of 77.23% were also fabricated to further reduce the Young's modulus of the TNTZ. According to the Relative Growth Rate (RGR) value, the as-printed TNTZ samples exhibited no cell cytotoxicity, where they showed even better biocompatibility than the comparative, as-printed Ti-6Al-4V samples. The as-printed TNTZ developed by the study demonstrates good biocompatibility, low stress shielding tendency and high mechanical properties.

1. Introduction

Biomedical titanium alloys have extensive medical applications due to their superior biocompatibility, excellent mechanical properties and low Young's modulus close to that of cortical bones [1–4]. Among the explored Ti-based biomaterials, Ti-6Al-4V has been widely used in making implant to replace shoulders, knees, elbows, or other body parts of the human being [5–7]. Recent research in biomedical titanium alloys, however, showed that novel β-type titanium alloys such as Ti-30Nb-5Ta-3Zr (TNTZ) [8–10] have better biocompatibility and lower stress shielding tendency, and thus were considered as more effective for promoting bone healing and remodeling than the Ti-6Al-4V alloy [11–13]. They were generally regarded as the next generation, more advanced metallic implant material [14–17].

For individual patient with e.g. bone loss or illness, standard mass production of implants may not meet their needs, and then the customized devices with geometry derives from the Magnetic Resonance Imaging (MRI) data was badly needed [18–20]. Selective Laser Melting (SLM), a powder bed based additive manufacturing technology, can be used to melt selected areas of each layer through a highly focused laser beam and under computer control; the final implants were obtained by accumulating layers [21–24]. Aside from dense implant, SLM can also fabricate customized implants with lattice structures, which allows the ingrowths of the new-bone tissues and transport of the body fluids [25–27]. Although some titanium alloys like commercially-pure Ti (CP-Ti) and Ti-6Al-4V have been successfully manufactured by SLM, few attempts have been devoted to the study of the processing, mechanical property and biocompatibility of Ti-30Nb-5Ta-3Zr manufactured by SLM [28,29]. During the SLM processing, heating & cooling rates of the metal material can reach to 10^5–10^6 K/s which could strongly affect the mechanical properties of the final material and finally effect the biocompatibilities [30–32].

In this work, samples of TNTZ with high relative density of 99.2% and TNTZ lattice structure samples with the porosity of 77.23% and Young's modulus of ~19.0 GPa were additively manufactured by SLM. The influences of the manufacturing strategy on the relative density and the Vickers hardness of the TNTZ alloy were discussed. The microstructure, elastic properties, fatigue properties and machining accuracy of the fabricated samples have been investigated. The biocompatibility of the as-printed TNTZ alloy has been investigated as well.

---

* Corresponding authors.
E-mail addresses: jfsun@hit.edu.cn (J.F. Sun), yanm@sustc.edu.cn (M. Yan).

https://doi.org/10.1016/j.msec.2018.11.077
Received 9 March 2018; Received in revised form 16 November 2018; Accepted 29 November 2018
Available online 30 November 2018
0928-4931/ © 2018 Elsevier B.V. All rights reserved.

Table 1
Chemical composition of TNTZ powders studied in this work (wt%).

Nb	Ta	Zr	O	Ti
30.4	5.28	7.16	0.11	Remainder

2. Materials and methods

2.1. Material preparation and characterization

The TNTZ powders were produced by Plasma Rotating Electrode Process (PREP; commercially purchased from Xiansailong Company), and the chemical composition of the powders was shown in Table 1(in wt%). The powder flowability was tested measured by the comprehensive characteristic tester of powder (BT-1000). Images of the TNTZ powders were acquired from the Tescan MIRA3 field-emission Scanning Electron Microscopy (SEM, operated at 10 kV, 60 μm aperture, and high current mode). The as-cast samples in this work were manufactured by arc melting. All 110 Titanium samples (both as-printed and as-cast, listed in Table 1) in this work were annealed (at 600 °C, 3 h) for stress relief [33,34].

A RENISHAW 250 HL machine equipped with a 200 W Yb:YAG pulsed fiber laser with a beam size of 80 μm was used to fabricate the samples under a high-purity Ar atmosphere containing no > 80 ppm environmental oxygen. TNTZ samples of $10 \times 10 \times 30\,\text{mm}^3$ dimension were additively manufactured through varying processing parameters including the point distance (PD, center distance between two molten pool; denoted as L, $L = 50$–$75\,\mu\text{m}$), laser exposure time (ET, time duration of single molten pool melted by laser spot; $T = 135$–$200\,\mu\text{s}$). The layer thickness (D, μm) was kept constant at 50 μm, and the laser power (P, W) was fixed at 200 W.

The relative density of samples was measured by the Archimedes' method. Then the "Best Parameter" was acquired. The Vickers hardness was measured on the polished samples through a microscopic Webster hardness Tester with a 500 N load and dwell time of 15 s (diamond indenter φ 2.8 mm). An average of 12 points was tested for each sample; the deviation in these measurements was less than ± 0.3%. The hardness on the sides showed 83%–92% of the top and shared the same trend as the top. However, due to the high value dispersion, the results were not included in our work.

Using the "Best Parameter", cylinder compression samples with Φ3 mm × 6 mm dimension were manufactured. Phase constitution was analyzed by the X-ray diffractometer (XRD, Rigaku Smartlab, Japan), with a Cu Kα radiation at 45 kV and 200 mA. Continuous scanning at a speed of 1.5 °/min was used from 2θ angle of 30° to 90°. The microstructure of the horizontal direction of the cube was examined by SEM, after the samples were etched with Kroll's Reagent (containing 100 mL water, 3 mL hydrogen fluoride and 5 mL nitric acid). The Electron Backscattered Diffraction (EBSD) mappings were also examined by the same SEM. The SEM mapping settings were 0.05 μm–0.5 μm step size and 1000–5000 grains with grain boundary definition as 10°. Grain size measurements were obtained using data for all grains in a single map.

The Young's modulus of the heat-treated samples (cylinder compression samples with Φ3 mm × 6 mm dimension) was measured by ultrasonic method on an ultrasonic velocity gauge (35 DL, Panametric, USA). A normal incident probe, model M110, 5 MHz and a shear probe, model V221, 5 MHz were used for the measurement of normal and shear velocities of the wave, respectively. Samples were compression-tested and tensile -tested using a microcomputer controlled universal testing machine (CMT 4503, MTS, USA) at a strain rate of $10^{-3}\,\text{s}^{-1}$. During the testing, the load–displacement data was recorded, and the Young's modulus was acquired. The samples of machining accuracy were also manufactured using the "Best Parameter" as well. After ultrasonic cleaned for 20 min, the samples were analyzed using SEM. The 3D morphological characterization of the as-printed samples was acquired through the Diondo-D2 micro-CT system. The surface roughness of the samples was measured by a 3-D profiler (Bruker, ContourTG-K0, Germany). Five measurements with a scan area of $0.09 \times 0.12\,\text{mm}^2$ were performed at random positions on 3 samples. The surface composition was analyzed using XPS (ESCALAB 250X), with an Al-K_α X-ray source (1486.6 eV) at a take-off angle of 90°. The stl. file of the lattice sample was generated by the MAGICS (Materialise, Leuven, Belgium), then the lattice sample were also additively manufactured by SLM (Table 2).

Table 2
List of TNTZ samples.

Kind of test	Print	Cast
Hardness	42	3
Compression	5	3
Tensile	5	3
Fatigue	30	–
EBSD	3	1
Biocompatibility	5	5
Lattice compression	5	–
Total	95	15

An Instron 8801 (USA) with 10 kN force cell was used to subject all fatigue samples to constant amplitude sinusoidal loading in compression-compression at fixed test frequency of 50 Hz and fixed load ratio R = 0.1. All experiments were force controlled and the stress-based approach was used for fatigue analysis. S-N curve was constructed by testing at least 5 identical samples at one stress amplitude.

2.2. Cell culture, proliferation

The SLMed samples were sliced and polished into 0.5 mm thick and 6.2 mm diameter discs. After high temperature sterilization, the discs were placed in 96-well TCPS (Tissue Culture Polystyrenes) plates. One of the control groups was the same culture medium but without the metal materials, while the rest control groups were the same culture medium filled with Ti-6Al-4V discs manufactured by SLM processing [35,36]. The blank group contained only PBS (Phosphate Buffered Saline, HyClone, USA) without cell suspension and materials. L929 cells (Mouse fibroblast cell line, purchased from the Shanghai Type Culture Collection, Chinese Academy of Sciences) were used for biocompatibility study and they were cultured at 37 °C and in a 5% CO_2 air atmosphere until cells were ready to be subcultured. After digesting with Trypsin-EDTA solution (0.25% Trypsin-0.53 mM EDTA solution), single-cell suspension was counted by Automated Cell Counter (Countess II, Invitrogen, USA). The cell suspension was diluted to a concentration of 1.0 × 104 cells/well. After preparation, 0.2 ml of the cell suspension was seeded into each well [37].

After cultured for 72 h, the discs were washed twice by PBS, and cell proliferation of each group was measured. 0.2 ml of fresh culture medium and 0.02 ml of CCK-8 (Cell Counting Kit-8, Dojindo, Japan) solution were added to each well and incubated at 37 °C for 2 h. Then the Optical Density (OD) value of the solution in each well was determined using the Varioskan LUX multimode microplate reader at a wavelength of 450 nm. Subsequently, cell Relative Growth Rate (RGR) was calculated by using the following method [38]:

$$\text{RGR} = [(A_s - A_b)/(A_c - A_b)] \tag{1}$$

where A_s was the OD value of experimental group, A_c was the OD value of control group and A_b was the OD value of blank group. The RGR value of the lattice structured TNTZ samples was obtained using the similar method in 6-well plates.

2.3. Cell morphology

The discs were cleaned twice with PBS, fixed with 4%

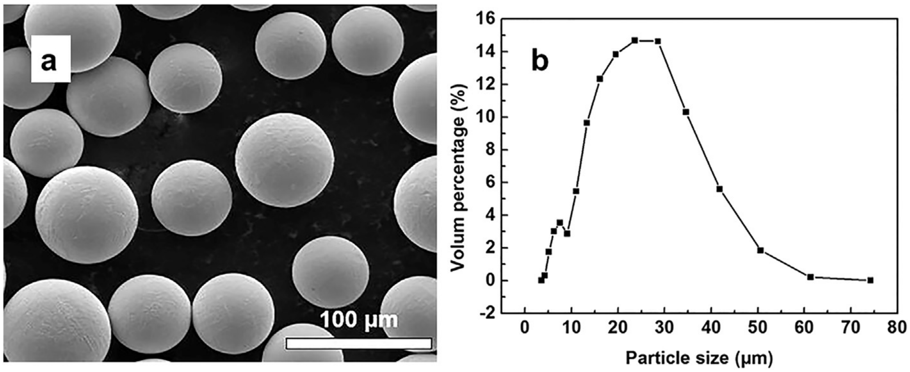

Fig. 1. (a) SEM image and (b) particle size distribution of the TNTZ powder.

paraformaldehyde for 30 min, stained with DAPI for 10 min, then cleaned twice with PBS again. The magnification fluorescence micrographs of the samples were acquired.

2.4. Statistical comparisons for the biocompatibility study

To further evaluation the biocompatibility, statistical comparisons were performed using Student's *t*-test for unpaired data. *P* values < 0.05 were considered significant for all tests [39].

3. Results

3.1. Powder characterization

Fig. 1 showed SEM image (Fig. 1a) and particle size distribution of the TNTZ powders (Fig. 1b). The powders were nearly spherical, and their size distribution followed Gaussian distribution with medium diameter of ~51 μm. Flowability test suggested that the powders showed angle of repose, angle of collapse, and apparent density as $\theta_r = 21.5^\circ$, $\theta_f = 19.2^\circ$, and 3.462 g/cm^3, respectively, suggesting excellent flowability of the powder (details were omitted here).

3.2. Porosity

Fig. 2 showed the effect of point distance (PD) and exposure time (ET) on the density of the SLMed samples. There was an overall trend of increasing relative density with decreasing PD down to 55 μm and with increasing ET up to 165 μs, after which level the density slightly decreased from 99.2% to 98.7%.

Regarding the effects of the point distance and the exposure time on the density, it was interpreted as follows: While decreasing laser input energy may cause less fusion and more porosity, increasing laser input energy was, on the other hand, likely to cause higher temperature in the molten pool. And once the powders were fully molten, too much melt convection, will, in turn, hinder the spreading of molten pool and cause the generation of pore defects. Indeed, other studies also showed that at shorter point distance (< 55 μm) or longer exposure time (> 165 μs), the balling, crack and oxide layer were generated in the melt pool, resulting in a poor layer surface and lower relative density [15].

Ignoring the laser transfer between the two adjacent molten pools, the laser scan speed can be approximated by the follows [40]:

$$v = L/t \tag{2}$$

where v was the laser scan speed (m/s), L was the point distance (μm) and t was the exposure time (μs). The corresponding scan speed of each data point in Fig. 3 were therefore calculated. The laser energy density

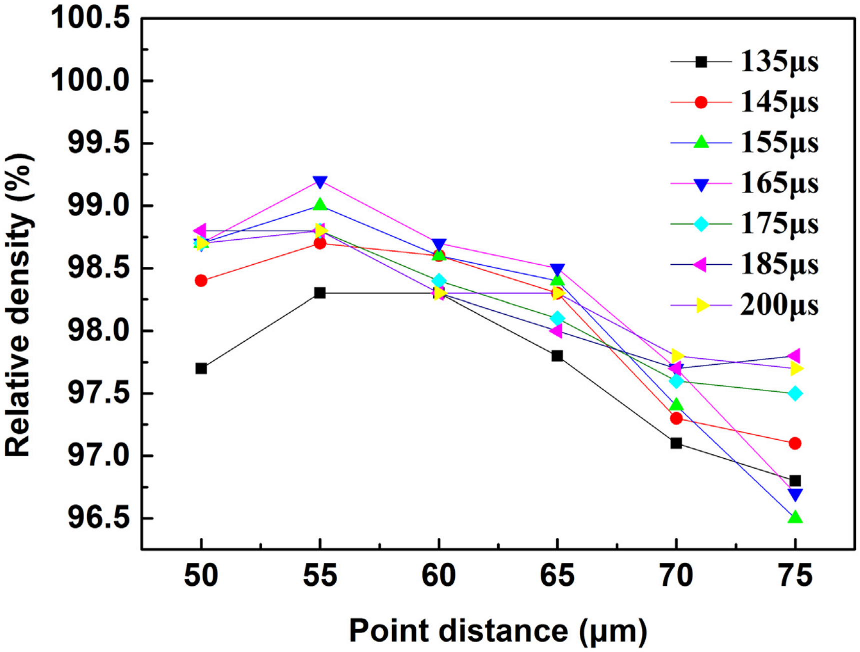

Fig. 2. Relative density of the 42 samples manufactured by SLM (laser power: 200 W; point distance: 50–75 μm; exposure time: 135–200 μs).

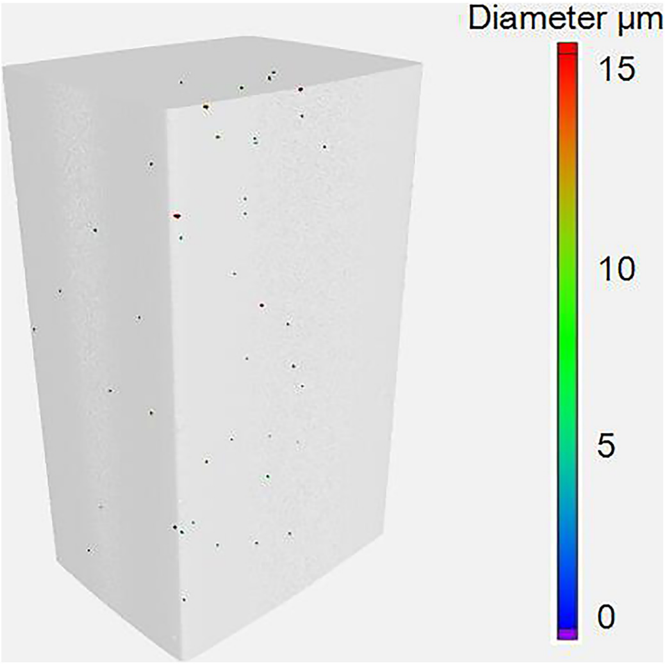

Fig. 3. The 3D, micro-CT image of the as-printed TNTZ.

(the total energy input per volume of each track), E (J/mm^3), can be calculated by [41]:

$$E = P/V \tag{3}$$

where P was the incident laser power (W) and V was the volume of laser scanned per second (mm^3/s). In this work, V can be estimated by:

$$V = v{\cdot}D{\cdot}(2L) \tag{4}$$

Then the energy density, E, can be calculated by:

$$E = PT/(2L^2D) \tag{5}$$

Based on Eq. (5), it was noted that L plays a major role on the resultant E. The laser energy density, E, was in turn a key factor that affects the quality of the SLMed samples. From Fig. 3, the "Best Parameter" was determined as PD: 55 μm, ET: 165 μs. The corresponding E of this point was about 109 J/mm^3, above or below which value porosity will increase.

Fig. 3 showed the 3D micro-CT image of the whole as-printed TNTZ sample. Merely few pores with a maximum diameter of ~15 μm can be found within the sample, and overall the as-printed sample showed almost near full density.

3.3. Microstructure study

Furthermore, results from X-ray diffraction (XRD) suggested that the SLMed TNTZ consisted of a majority β phase and a minority α phase (Fig. 4a). Fig. 4b revealed that the as-built struts were filled with very fine α′ martensitic laths (average length 0.8 μm). Again, the microstructure showed no obvious apparent porosity. The EBSD results of the horizontal plane (XOY plane) (Fig. 5a) suggested that the average grain size of as-printed sample is ~17.6 μm, 9 times smaller than the as-cast sample (~157.4 μm; Fig. 5b).

3.4. Mechanical properties of the SLMed TNTZ alloy

All hardness samples were well polished, the 3-D profiler image of one sample (Fig. 6a) showed that the roughness of the samples was Ra ~0.043 μm. Fig. 6b showed the Vickers hardness at different DP or ET. Among the tested 42 samples, 32 samples exhibited higher hardness than the control samples prepared by arc melting (~279.4 HV). Along with the increasing of relative density, Vickers hardness of the samples showed an increasing tendency. At relative density of > 99.2%, the hardness reaches up to 305.4 HV and then tends to a plateau. The overall tendency of hardness similar to the one of the as-printed density. Combining the density results and the hardness results, the appropriate laser energy density ranges 109 J/mm^3–133 J/mm^3.

Due to the excellent ductility, both as-printed and as-cast TNTZ samples were not fully fractured in the compression test (Fig. 7a, b). Part of the typical compression stress–strain curve of the as-printed sample was shown, with a comparative curve from as-cast TNTZ. The as-printed and as-cast samples exhibited Young's modulus of 59.5 GPa and 83.2 GPa, respectively; their yield strength was 664 MPa, and 736 MPa, respectively. Compared to the fully-dense as-cast TNTZ, although the as-printed TNTZ appears lower yield strength, the value was still much higher than CP-Ti [1]. More importantly, the as-printed TNTZ showed lower Young's modulus compared to the as-cast TNTZ and this was preferred from reducing stress shielding perspective. Fig. 7c showed the typical tensile stress–strain curve of the as-printed samples. It was noted that the as-printed TNTZ showed a highest tensile strength (~680 MPa) and a lower Young's modulus (~64.2 GPa). The corresponding elongation was ~15.3%. Compared the data of as-cast TNTZ from the literature [42] (tensile strength at 680–720 MPa, Young's modulus at ~82 GPa and elongation at ~8–10%), the as-printed TNTZ showed slightly lower in tensile strength, but much higher in elongation. It was noted that the strengthening mechanism of the as-printed samples was considered as fine grain strengthening which improved the as-printed samples' elongation (the average grain size: as-printed sample ~ 17.6 μm, as-cast sample ~ 157.4 μm; Fig. 5) and the density of samples has played a dominant role to its mechanical properties which decreased the tensile strength. The fracture surface morphology was observed by SEM in order to identify the ductile fracture and some ductile dimples, as shown in Fig. 7d. The fracture surface showed little size of voids and unmelted powder particles. The defects including voids were always considered as the parts to trigger a failure in the tensile process and the decreasing of young's modulus [43]. In addition, the unmelted powder particles existing in the small

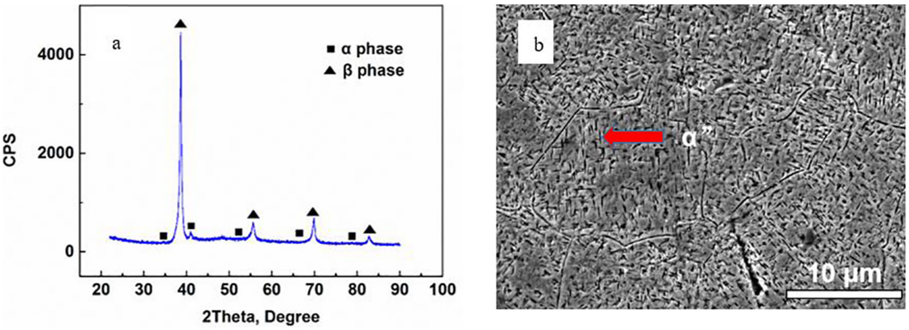

Fig. 4. (a) XRD result; (b) metallograph of the TNTZ sample (laser power: 200 W; point distance: 55 μm; exposure time: 165 μs).

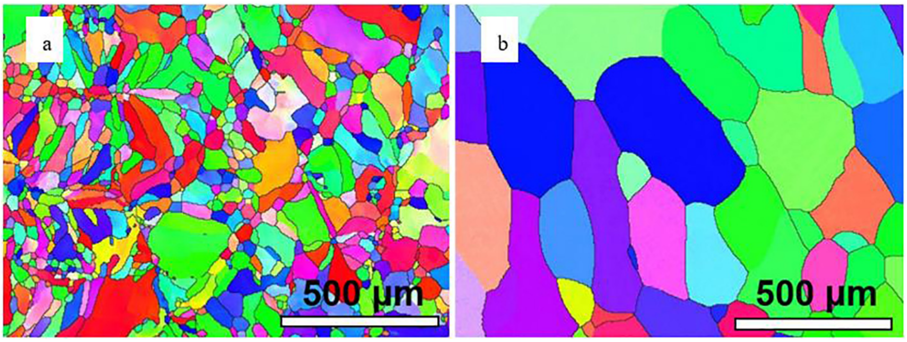

Fig. 5. EBSD image of (a) as-printed sample; (b) as-cast sample.

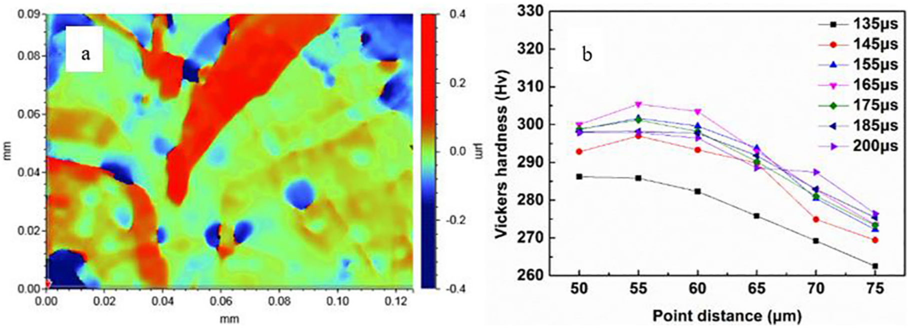

Fig. 6. (a) 3-D profiler image of one polished hardness sample, (b) Vickers hardness (Hv) of the samples manufactured by SLM as a function of point distance at a laser powder of 200 W, point distance of 75–50 µm, and exposure time of 135–200 µs.

voids (marked by arrow in Fig. 7d) were attributed to the incomplete melting under insufficient laser irradiation. The fracture surface microstructure was presented the ductile dimples. Compared with the tensile test, the low modulus measured in the compression test may be due to the error caused by the extensometer not being directly loaded onto the upper and lower surface of the compressed sample. The average value of the Young's modulus of as-printed and as-cast TNTZ samples obtained by ultrasonic technique was 62.8 ± 1.6 GPa and 83.7 ± 1.87 GPa, respectively. It was further proved that SLM technology can prepare TNTZ alloy with lower Young's modulus.

The as-printed TNTZ fatigue sample was shown in Fig. 8a (Ra 0.054 µm) and the S-N curve was shown in Fig. 8b. According to the results acquired in this work, considering the non-linear S-N model from literature [44], the S-N equation of the as-printed TNTZ was

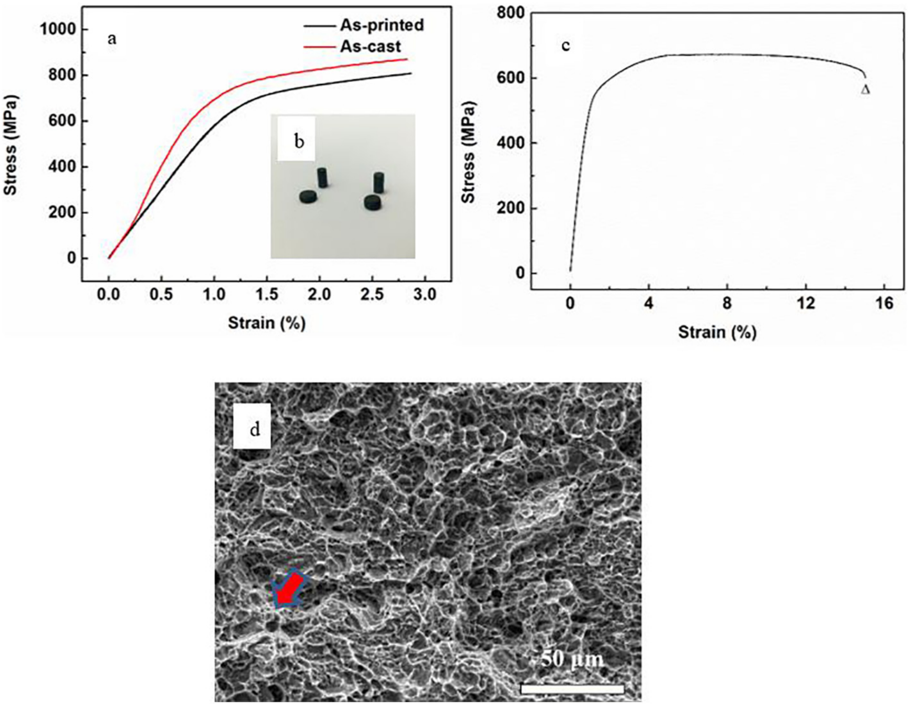

Fig. 7. (a) Compression stress–strain curves, (b) as-printed and as-cast TNTZ compression samples, (c) tensile stress–strain curves, (d) fracture surface morphologies.

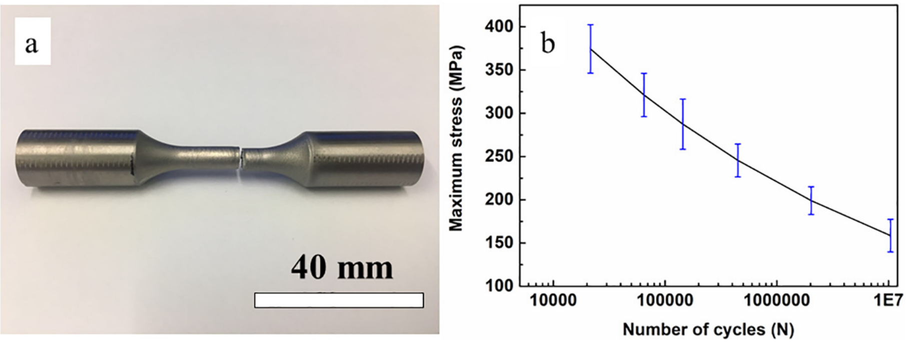

Fig. 8. (a) TNTZ fatigue sample, (b) S-N curve of as-printed TNTZ sample.

proposed as follows:

$$\log N + 7.2 \log S = 22.86 \tag{6}$$

where S, and N were maximum stress and number of cycles. It could be seen from the Fig. 8b that the fatigue limit of as-printed TNTZ was ~140 MPa (10^7 Nf). Compared the data of as-cast TNTZ from the literature [45] (fatigue limit 330 MPa), the as-printed TNTZ showed much lower in fatigue limit, but still higher than the cortical bone (fatigue limit 80 MPa [46]). The defects including voids were considered as the parts to decrease the fatigue limit. According to the literature [47], Hot Isostatic Pressing (HIP) can further increase the relative density, fatigue limit and the yield strength of as-printed TNTZ alloy.

3.5. Biocompatibility of the SLMed TNTZ

After 72 h culture, the cell morphologies on the as-printed TNTZ and TCPS were shown in Fig. 9a, c. Similar cell shape and spreading behavior was observed. In comparison with the as-printed TNTZ, the cells cultured on the as-printed Ti-6Al-4V alloys (Fig. 9b) exhibit a near-round shape with less spreading. The results suggested that the cells were almost reached a complete adhesion. According to the corresponding standard (GB/T16886.5- 2003 [48]), the proliferation rates of L929 cells on the three sample surfaces were evaluated by the CCK-8 method, and the RGR value was shown and compared in Fig. 10. The results showed that the RGR of L929 cells were 92.76%, and 84.03% for the as-printed TNTZ and Ti-6Al-4V, respectively, and the cytotoxicity levels of both samples were of Grade 1 for biomedical materials. On the other hand, the cell viability on the TNTZ alloys and TCPS was significantly higher than that on the Ti-6Al-4V alloys. These results indicated that all samples appear no cell cytotoxicity according to the RGR value, and the as-printed TNTZ sample appears better biocompatibility than the Ti-6Al-4V alloy, suggesting that the as-printed TNTZ can be superior biomedical implant materials.

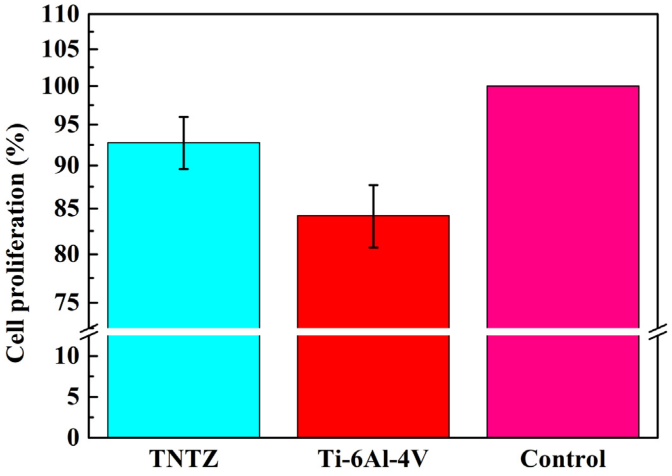

Fig. 10. RGR of L929 cells after 72 h culture.

4. Discussion

4.1. Discussion on Young's modulus of the SLMed TNTZ

The yield strength and Young's modulus of some typical biomedical titanium alloys [49–51], together with the as-printed TNTZ of this study, were shown in Fig. 11. Among all the compared Ti and Ti alloys, the TNTZ alloy exhibited low Young's modulus and the as-printed TNTZ alloy exhibited even lower Young's modulus, which was much closer to the cortical bone.

For further reducing the Young's modulus and making it match that of the e.g. the cortical bone structure, lattice structure of the TNTZ alloy could be made using MAGICS file (lattice name: rhombic dodecahedron) and manufactured by SLM. It was generally accepted that the relationship between compressive properties and relative density, e.g. the Gibson–Ashby model [52] suggesting:

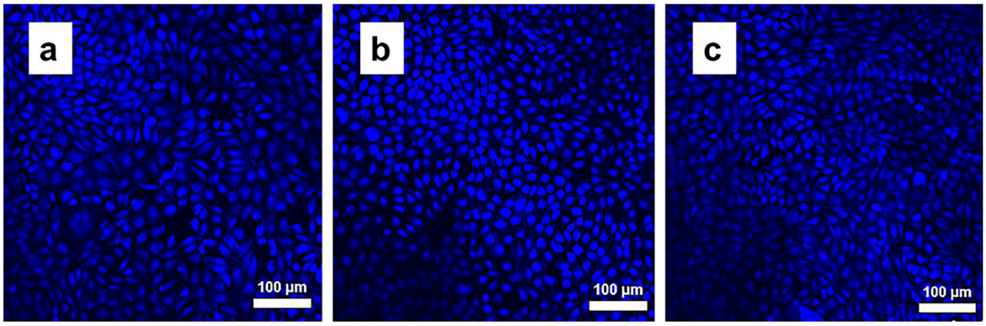

Fig. 9. L929 cells morphology on (a) as-printed TNTZ alloy, (b) as-printed Ti-6Al-4V alloys, and (c) TCPS.

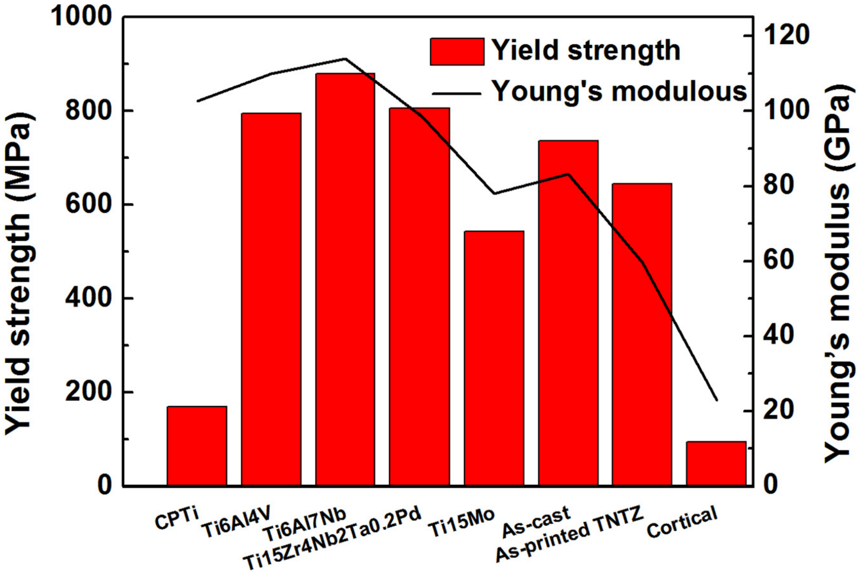

Fig. 11. The yielding strength and Young's modulus of some typical medical titanium alloys.

$$\log\left(\frac{E}{E_s}\right) = C_1 + n_1 \log\left(\frac{\rho}{\rho_s}\right) \tag{7}$$

$$\log\left(\frac{\sigma_y}{\sigma_{ys}}\right) = C_2 + n_2 \log\left(\frac{\rho}{\rho_s}\right) \tag{8}$$

where E, σ_y and ρ/ρ_s were Young's modulus, yield stress and relative density of porous metals, respectively. E_s and σ_{ys} were Young's modulus and yield stress of solid metals, respectively. C_1 and C_2 are constants related to materials. n_1 and n_2 are exponents related to pore structure.

Based on this, high porosity lattice structure with 77.23 vol% porosity was produced (Fig. 12). Through creasing porosity, the integral Young's modulus of the lattice structure was reduced to 0.79 GPa. Fig. 12a showed that, due to the excellent ductility, the lattice samples were not fully fractured in the compression test. The compressive curve was shown in Fig. 13a. The integral Young's modulus of the as-printed lattice samples can be lowed to ~0.79 GPa These results suggested that the integral Young's modulus value of the as-printed TNTZ lattice/dense samples range was at least in the range of 0.79–64.2 GPa. Fig. 13a also indicated that the integral yield strength of the lattice samples was ~15.7 MPa, which meant that the integral yield strength value of the as-printed TNTZ lattice/dense samples range was at least in the range of 15.7–520 MPa (Fig. 7c), which perfectly covers all possible ranges of human cortical bone [53]. Image of Fig. 13b indicated that there were still little porous defects could be found in the as-printed lattice sample. These defects can be eliminated to increase the integral yield strength of the lattice samples through the post-processing like HIP [46]. Above all, the integral Young's modulus and integral yield strength could be tailored to suit human bone properties, by designing the amount of porosity with appropriate processing parameters, and it became the next step of our work.

On the other hand, regarding preparing lattice structure, we have noted that the capability of making fine holes for the lattice structure and maintaining the printing accuracy needs to be carefully tested. Fig. 14 illustrated that to make fine-scale samples, the minimum joint size, and the minimum pore size was ~300 μm, and ~400 μm, respectively, for the SLM facility currently used. The SEM images of dimensional accuracy samples were shown in Fig. 14. Fig. 14a showed the boundary of 300 μm joint was smoother and clearer. Optical measurement (Fig. 14b) demonstrates that the absolute error was kept at 6–7 μm, and the relative error decreased with the increasing of the design size. Fig. 14c showed the boundaries of Φ500 μm were of accuracy. Fig. 14d demonstrated that the absolute error increased with the decreasing of the design size, and the relative error increased significantly when the design size increased down to 300 μm. According to the literature [54], implants with pore sizes of 400–600 μm exhibited healing of femoral defects in rats. The accuracy result showed that fine scaled lattice structure with 400 μm pore size can be manufactured for the SLM facility currently used. Thus, 400 μm was finally chosen to be the pore size.

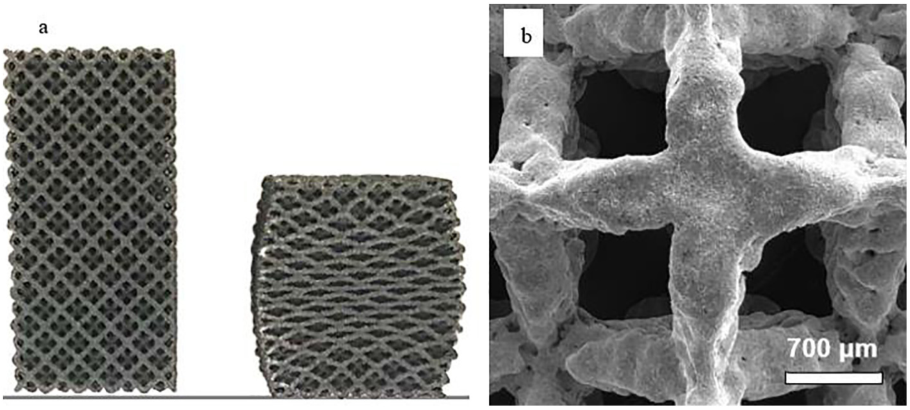

Fig. 12. (a) Optical image, (b) SEM image optical image of the lattice sample produced at PD: 55 μm; ET: 165 μs.

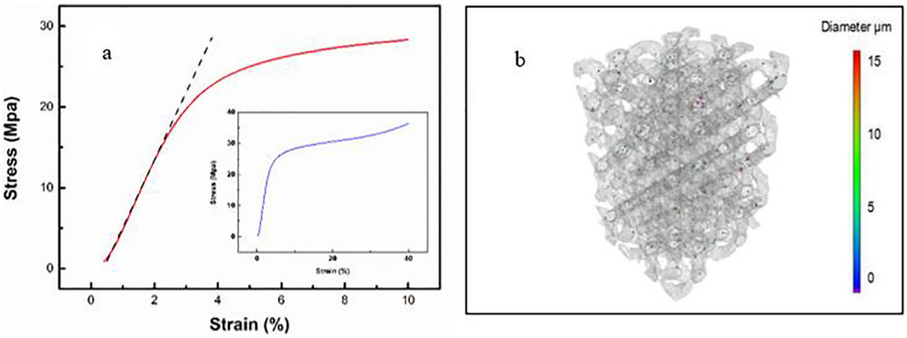

Fig. 13. (a) Compression curve (b) micro-CT image of the lattice TNTZ sample.

4.2. Discussion on the biocompatibility of the SLMed TNTZ

By evaluating their RGR values, the as-printed samples generally showed better biocompatibility than the as-cast samples, in this work. One of the reasons causing the differences between the as-printed and the as-cast was likely because a higher surface roughness was observed for the as-printed samples.

A Bruker 3-D profiler was used to measure the surface roughness of the samples. The 3-D profiler images (Fig. 15a, b) and the average surface roughness (Fig. 15c) were showed in Fig. 15. Fig. 15c, represents the expected smooth surface for the as-cast sample. While the effect of metallurgical defects or voids (dark dot in Fig. 15b) increased the surface roughness for the as-printed sample. Due to the higher surface roughness and enlarged surface area of the as-printed sample, the as-printed sample can adsorb more proteins mediate cell adhesion than the as-cast ones [55,56]. This was likely the reason that the as-printed sample exhibits better bioactivity than the as-cast sample by RGR value.

The as-printed TNTZ samples appeared excellent biocompatibility. This was not only because the lower modulus or the surface roughness of the alloy which has less chance to cause stress shielding, but also because the non-toxic and non-allergic elements contained in the alloy [22–26].

Fig. 16a showed the XPS survey spectra at binding energies (BEs) of 0–1250 eV for the TNTZ sample, which was sputtered using an Ar-ion beam for 0 s. In addition to the expected elements such as Ti, Nb, Ta, Zr and O, additional peaks from C was also detected, which were most likely introduced during sample preparation. XPS results (Fig. 16b) showed that the as-printed TNTZ samples have TiO_2 film on the surface, which was key to the biocompatibility of biomedical Ti alloys [57,58]. However, SLM processing could make the as-printed TNTZ samples show differences in protein adsorption and cell behavior compared to the conventional TiO_2 films. The cell behavior on the as-printed TNTZ samples needs further research.

5. Conclusions

- Biomedical β-type Ti-30Nb-5Ta-3Zr alloy has been prepared using SLM. Near full density samples (99.2% relative density) have been obtained at a point distance of 55 µm, an exposure time of 165 µs,

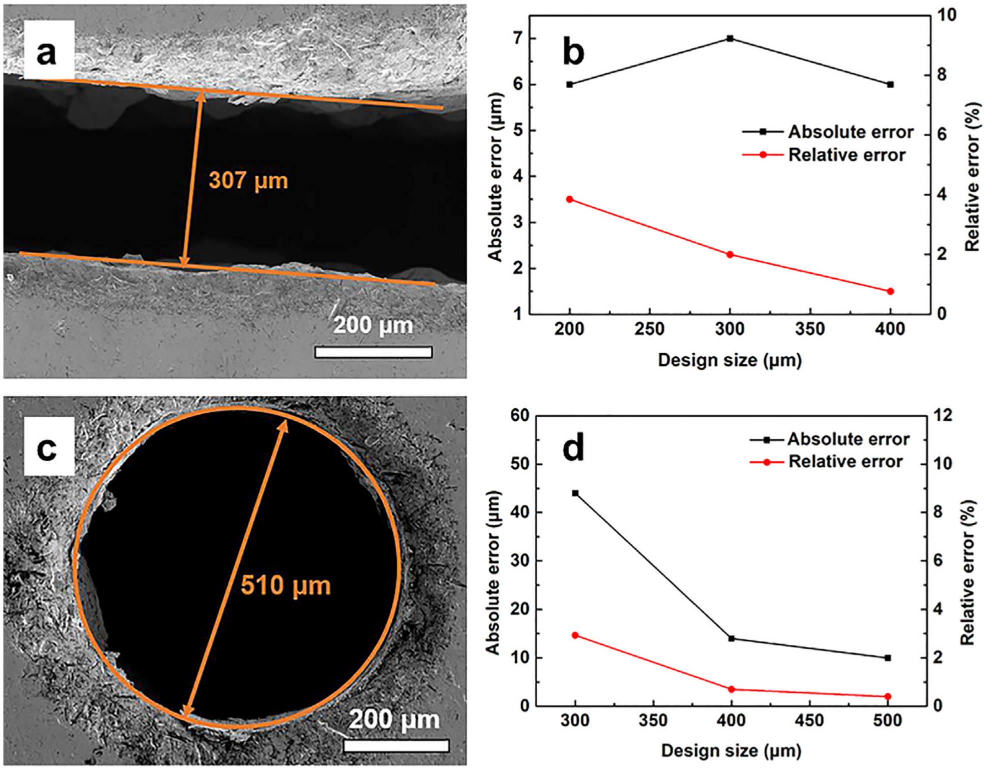

Fig. 14. SEM images of the joints sample produced at PD: 55 µm; ET: 165 µs. (a) 300 µm joint, (b) dimensional error analysis of joints, (c) Φ500 µm hole, (d) dimensional error analysis of hole.

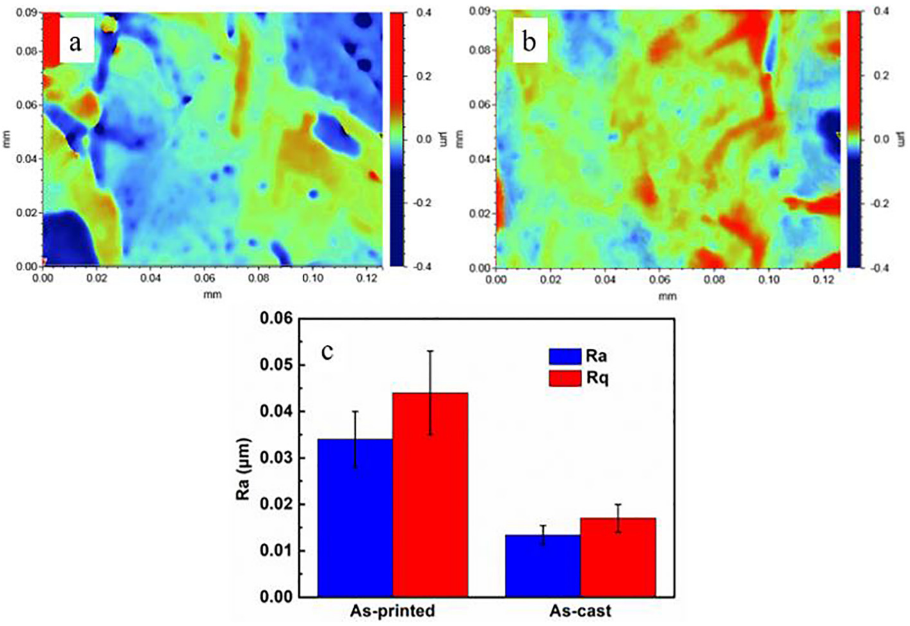

Fig. 15. 3-D profiler images of (a) as-printed TNTZ, (b) as-cast TNTZ and (c) the average surface roughness.

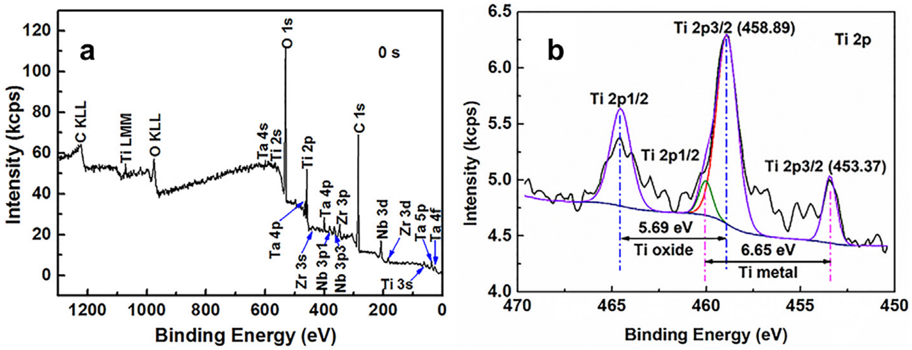

Fig. 16. XPS fine analyses of the as-printed TNTZ samples.

and 50 μm layer thickness using 200 W pulsed laser.

- The tensile strength, Young's modulus, elongation and fatigue limit of the as-printed TNTZ was ~680 MPa, ~64.2 GPa, ~15.3% and ~140 MPa. The non-linear S-N equation of the as-printed TNTZ was proposed. By creating lattice structure of 77.23 vol% porosity, the integral yield strength value of the as-printed TNTZ lattice/dense samples range was acquired (15.7–520 MPa), which perfectly covers all possible ranges of human cortical bone.
- According to the biocompatibility evaluation and the RGR value, the SLMed TNTZ appears no cell cytotoxicity and it's showed better biocompatibility than Ti-6Al-4V.
- The results of the present study suggest that SLM was capable to produce low-E advanced TNTZ alloy with excellent biocompatibility and minimum stress shielding tendency.

Acknowledgments

This research was funded by [Shenzhen Science and Technology Innovation Commission grant number ZDSYS201703031748354 and JCYJ20170817110331228], the National Natural Science Foundation of China [project No. 51604104] and Natural Science Foundation of Guangdong Province [grant number 2016A030313756]. This work was also supported by the Pico Center at SUSTech with support from the Presidential fund and Development and Reform Commission of Shenzhen Municipality. Dr M. Yan appreciates the support by the Humboldt Research Fellowship for Experienced Researchers.

References

[1] X. Liu, P.K. Chu, C. Ding, et al., Mater. Sci. Eng. R 47 (3) (2004) 49–121.
[2] K. Maekawa, Y. Yoshida, A. Mine, et al., J. Biomed. Mater. Res. A 82 (1) (2007) 195–200.
[3] L. Hu, S. Guo, Q. Meng, et al., Metall. Mater. Trans. A 45 (2) (2014) 547–550.
[4] M. Nakai, M. Niinomi, X. Zhao, et al., Mater. Lett. 65 (4) (2011) 688–690.
[5] D.G. Robertson, H.B. Mcshane, Met. Sci. J. 13 (7) (2013) 575–583.
[6] C. Kurzmann, K. Janjić, H. Shokoohitabrizi, et al., Theatr. Res. Int. (8) (2017) 1–11.
[7] M. Akita, Y. Uematsu, T. Kakiuchi, et al., Mater. Sci. Eng. A 627 (2015) 351–359.
[8] J.H. Kim, Y.U. Sim, T.Y. Yang, et al., J. Kor. Ceram. Soc. 47 (2) (2010) 127–131.
[9] L.C. Zhang, D. Klemm, J. Eckert, et al., Scr. Mater. 65 (1) (2011) 21–42.
[10] J. Xiao, H. Zhou, L. Zhao, et al., Osteoporos. Int. 22 (6) (2011) 1907–1913.
[11] A. Sak, T. Moskalewicz, S. Zimowski, et al., Mater. Sci. Eng. C 63 (2016) 52.
[12] S. Sathish, M. Geetha, S.T. Aruna, et al., Ceram. Int. 37 (4) (2011) 1333–1339.
[13] M.W. Mendes, C.G. Ágreda, A.H. Bressiani, et al., Mater. Sci. Eng. C 63 (2016) 671.
[14] Y.-D. Im, Y.-K. Lee, K.-H. Song, Mater. Sci. Eng. A 725 (16) (2018) 479–487.
[15] S.L.G. Petroni, M.S.M. Paula, V.A.R. Henriques, et al., Powder Metall. 56 (3) (2013) 202–207.
[16] J. Szewczenko, J. Marciniak, W. Kajzer, et al., Arch. Metall. Mater. 61 (2) (2016) 695–700.
[17] J. Hwang, J.S. Dufour, G.G. Knapik, et al., Clin. Biomech. 37 (2016) 60–64.
[18] S. Lachmann, J.Y. Laval, D. Axmann, et al., Int. J. Oral Maxillofac. Implants 26 (2) (2016) 347.
[19] L.E. Wright, A.A. Harhash, W.M. Kozlow, et al., Oncotarget 8 (5) (2016) 8406.
[20] S. Casimiro, I. Alho, M. Bettencourt, et al., J. Bone Oncol. 2 (3) (2013) 116.
[21] Y.H. Zhou, S.F. Lin, Y.H. Hou, et al., Appl. Surf. Sci. 441 (2018) 210–217.
[22] J.J. Yan, D.L. Zheng, H.X. Li, et al., J. Mater. Sci. 52 (2017) 12476–12485.
[23] M. Mazur, M. Leary, M. Mcmillan, et al., Laser Additive Manuf. (2017) 119–161.
[24] M. Ma, Z. Wang, X. Zeng, Mater. Sci. Eng. A 685 (2016) 265–273.

[25] X.P. Li, K.M. O'Donnell, T.B. Sercombe, Addit. Manuf. 10 (2016) 10–14.
[26] J. Vaithilingam, R.D. Goodridge, R.J.M. Hague, et al., J. Mater. Process. Technol. 232 (September) (2016) 1–8.
[27] X. Suyalatu, N. Takayoshi, H. Norio, et al., Front. Bioeng. Biotechnol. 4 (2016).
[28] L. Yan, Y. Yuan, L. Ouyang, et al., J. Alloys Compd. 688 (2016) 156–162.
[29] L. Yan, J. Yu, X. Zhang, et al., Nanosci. Nanotechnol. Lett. 9 (3) (2017) 322–327.
[30] H.B. Van, Y. Apers, K. Lietaert, et al., Acta Biomater. 47 (2016) 193–202.
[31] T. Ma, X.Y. Song, W.J. Ye, et al., Mater. Sci. Forum 849 (2016) 281–286.
[32] H.J. Gao, Y.D. Zhang, Q. Wu, et al., Metals Open Access Metall. J. 7 (5) (2017) 158.
[33] D. Bogdanski, M. Koller, D. Muller, et al., Biomaterials 23 (23) (2002) 4549–4555.
[34] M.A. Baker, S.L. Assis, O.Z. Higa, et al., Acta Biomater. 5 (1) (2009) 63.
[35] T. Walenda, S. Bork, P. Horn, et al., J. Cell. Mol. Med. 14 (1–2) (2010) 337–350.
[36] Małgorzata Osękowska, Ewa KarugaKuźniewska, Damian Wojcieszak, et al., Pol. J. Chem. Technol. 17 (3) (2015) 33–39.
[37] P. Karimi, T. Raza, J. Andersson, et al., Int. J. Adv. Manuf. Technol. 1–2 (2017) 1–9.
[38] Abdullah Yahia Alfaify, James Hughes, Keith Ridgway, et al., Addit. Manuf. (2018) 197–204.
[39] X. Yang, K. Yang, S. Wu, et al., Radiat. Phys. Chem. 79 (5) (2010) 606–611.
[40] G. He, M. Hagiwara, Mater. Sci. Eng. C 25 (3) (2005) 290–295.
[41] J.M. Calderon Moreno, C. Vasilescu, S.I. Drob, et al., Mater. Corros. 65 (7) (2014) 703–714.
[42] P. Majumdar, S.B. Singh, M. Chakraborty, Mater. Sci. Eng. A 223 (2) (2008) 419–425.
[43] I. Yadroitsava, S. Grewar, D. Hattingh, et al., Mater. Sci. Forum 828 (2015) 305–310.
[44] Davide Leonetti, Johan Maljaars, H.H. (Bert) Snijder, Int. J. Fatigue 105 (2017) 128–143.
[45] T. Akahori, T. Hattori, T. Yasui, et al., Frontiers in Bioengineering, Biotechnology 4 (2016).
[46] C.A. Pattin, Caler, D.R. Carter, J. Biomech. 29 (1996) 69–79.
[47] B. Vayssette, N. Saintier, C. Brugger, et al., Procedia Eng. 213 (2018) 89–97.
[48] X. Li, C.T. Wang, W.G. Zhang, et al., Proc. Inst. Mech. Eng. H J. Eng. Med. 489 (2009) 173–181.
[49] T. Lee, M. Nakai, M. Niinomi, et al., Met. Mater. Int. 21 (1) (2015) 202–207.
[50] Y. Kirmanidou, M. Sidira, M.E. Drosou, et al., Biomed. Res. Int. 2016 (2) (2016) 2908570.
[51] M. Niinomi, J. Mech. Behav. Biomed. Mater. 1 (1) (2008) 30–42.
[52] Fuping Li, Jinshan Li, Hongchao Kou, et al., J. Mater. Sci. Technol. 32 (2016) 937–943.
[53] Yener N. Yeni, David P. Fyhrie, J. Biomech. 36 (2003) 1343–1353.
[54] E. Damien, K. Hing, S. Saeed, et al., J. Biomed. Mater. Res. A 66 (2003) 241–246.
[55] S. Yu, B. Wang, Y. Pan, et al., J. Clean. Prod. 176 (2018) 636–644.
[56] D. Yang, X. Lü, Y. Hong, et al., Biomaterials 35 (2014) 6195–6205.
[57] X. Wang, F. Prokert, H. Reuther, et al., Surf. Coat. Technol. 185 (1) (2004) 12–17.
[58] M. Niinomi, M. Nakai, J. Hieda, et al., Acta Biomater. 8 (11) (2012) 3888–3903.